



# The Use of Acoustic Emission to Characterize Fracture Behavior During Vickers Indentation of HVOF Thermally Sprayed WC-Co Coatings

N.H. Faisal, J.A. Steel, R. Ahmed, and R.L. Reuben

(Submitted January 20, 2009; in revised form April 14, 2009)

This paper describes how acoustic emission (AE) measurements can be used to supplement the mechanical information available from an indentation test. It examines the extent to which AE data can be used to replace time-consuming surface crack measurement data for the assessment of fracture toughness of brittle materials. AE is known to be sensitive to fracture events and so it was expected that features derived from the AE data may provide information on the processes (microscale and macroscale fracture events and densification) occurring during indentation. AE data were acquired during indentation tests on samples of a WC-12%Co coating of nominal thickness 300  $\mu\text{m}$  at a variety of indentation loads. The raw AE signals were reduced to three stages and three features per stage, giving nine possible indicators per indentation. Each indicator was compared with the crack profile, measured both conventionally and using a profiling method which gives the total surface crack length around the indent. A selection of the indents was also sectioned in order to make some observations on the subsurface damage. It has been found that reproducible AE signals are generated during indentation involving three distinct stages, associated, respectively, with nonradial cracking, commencement of radial cracking, and continued descent of the indenter. It has been shown that AE can give at least as good a measure of cracking processes during indentation as is possible using crack measurement after indentation.

**Keywords** acoustic emission, fracture toughness, HVOF, surface crack length, Vickers indentation, WC-12%Co coating

## 1. Background

Various authors have used crack patterns at, and beneath, the surface of indentations to assess the fracture toughness of ceramics (Ref 1-6), study the hardness of plasma-sprayed coatings (Ref 7-9), and evaluate the residual stress, adhesive strength, and fracture toughness of thermally sprayed high velocity oxygen fuel (HVOF) cermet coatings (Ref 10-14). However, there has been no work on microfissuring of sprayed HVOF coating materials during the indentation process.

Acoustic emission (AE) is a nondestructive technique that has been used to monitor damage processes in engineering materials (Ref 15), as well as for condition monitoring (Ref 16, 17). It is well-established that crack extension processes give rise to AE which can be recorded using sensors placed on the surface of the

structure or sample of interest. There have been some limited studies of the use of AE to study fracture during indentation, for example by Safai et al. (Ref 18), who found the total AE event count during Brinell indentation tests to be related to the porosity of plasma-sprayed alumina coatings. They noted that the high critical loads for this particular coating-substrate couple were not enough to generate de-bonding at the interface during indentation, but they suggested that some of the AE sources might be due to mechanically induced closure of pores. Ajit Prasad et al. (Ref 19), working on plasma-sprayed alumina-titania coating systems, suggested that the AE signal associated with plastic deformation during indentation is of a more continuous type with a lower characteristic frequency content (35-40 kHz), whereas the instantaneous relaxation associated with cracking produces burst type AE signals with a characteristic frequency in the range 220-280 kHz. Vijayakumar et al. (Ref 20) have found the frequency of the AE signal associated with impact indentation (at 20 kHz) to be in the range of 200-400 kHz for the as-sprayed coatings and 800-900 kHz plasma-sprayed alumina-titania coatings with and without subsequent microwave treatment, respectively. Finally, Senturk et al. (Ref 21) found that the presence of a bond coat layer of NiCrAl in partially stabilized, plasma-sprayed zirconia ceramic coatings suppresses AE activity during Hertzian indentation, and attributed this to surface compressive stresses inhibiting cracks. Thus, there is some evidence that AE is associated with the indentation of

N.H. Faisal, J.A. Steel, R. Ahmed, and R.L. Reuben, Department Mechanical Engineering, School of Engineering and Physical Sciences, Heriot-Watt University, Edinburgh EH14 4AS, UK. Contact e-mail: R.Ahmed@hw.ac.uk.

Nomenclature			
$a_{1,2}$	Vickers indentation size for half diagonal 1 and 2	$t$	time
$a$	average Vickers indentation half diagonal size	$T$	acoustic emission event duration
$c_{1,2}$	radial crack length along Vickers indentation diagonal 1 and 2	$T_i$	individual acoustic emission event duration
$c$	average radial crack length $c = l + a$	$V$	voltage
$E$	acoustic emission energy	$V_{abs}$	absolute voltage
$HV$	Vickers hardness	$x_n$	serrated crack path unit length
$k_1$	fracture toughness empirical constant	$X$	fracture toughness variable
$K_{AE}$	acoustic emission-based fracture toughness	<b>Subscript</b>	
$K_{1c}$	fracture toughness	$i$	initial value
$l_a$	average surface radial crack length	$N$	final value
$l_{yn}$	crack path unit length	$n$	resolvable crack length
$L$	total surface crack length	$y$	number of cracks
$P$	indentation load	<b>Abbreviations</b>	
$R$	acoustic emission ring-down count	AE	acoustic emission
$R_a$	average surface roughness	HVOF	high velocity oxygen fuel
$r$	linear correlation coefficient		

coatings and that some of the time-frequency characteristics differ with different accommodation mechanisms and coatings.

Here, the primary aim was to find a method of recognizing and characterizing automatically the indentation fracture pattern and critical load in HVOF coatings with a view to providing an indirect measure of fracture toughness. This would allow a test to be applied quickly and efficiently, perhaps as an adjunct to the manufacturing process, and perhaps with better resolution than can be obtained by measurement of surface cracks. The work relies on the semi-empirically established proportionality between surface crack length and fracture toughness, and therefore seeks to establish the relationship between surface cracking and AE. For this reason, the study was confined to a single coating type, hence a single fracture toughness, and the indentation load was varied to vary the degree to which the coating needs to accommodate the indenter.

## 2. Experimental Apparatus and Procedure

The experiments essentially consisted of producing indentations using a conventional Vickers hardness testing machine at 10 different loads between 49 and 490 N with a single AE sensor mounted on the surface. Five indentations were produced at each load and the surface cracking pattern was subsequently measured for all indentations. A limited number of indentations were examined for detailed surface and subsurface damage using scanning electron microscopy.

### 2.1 Specimen Details

The three test specimens used in this study were as-sprayed HVOF WC-12%Co thermally sprayed onto substrates consisting of 440C stainless steel discs of diameter

31 mm and thickness 8 mm. The microhardness of the coatings normal to the surface was found to be  $1050 \pm 70$  HV<sub>196N</sub> (average of 15 indentations). The spraying was done using the HVOF (Jet-kote) process following commercial procedures to produce a coating thickness of between 300 and 325  $\mu\text{m}$ . In preparation for the indentation test, each sample was polished to a surface roughness  $R_a = 0.043 \pm 0.01$   $\mu\text{m}$ , using, consecutively, 6, 1, and 0.5  $\mu\text{m}$  diamond paste in a process known to present to the indenter a uniform coating structure and morphology (Ref 22).

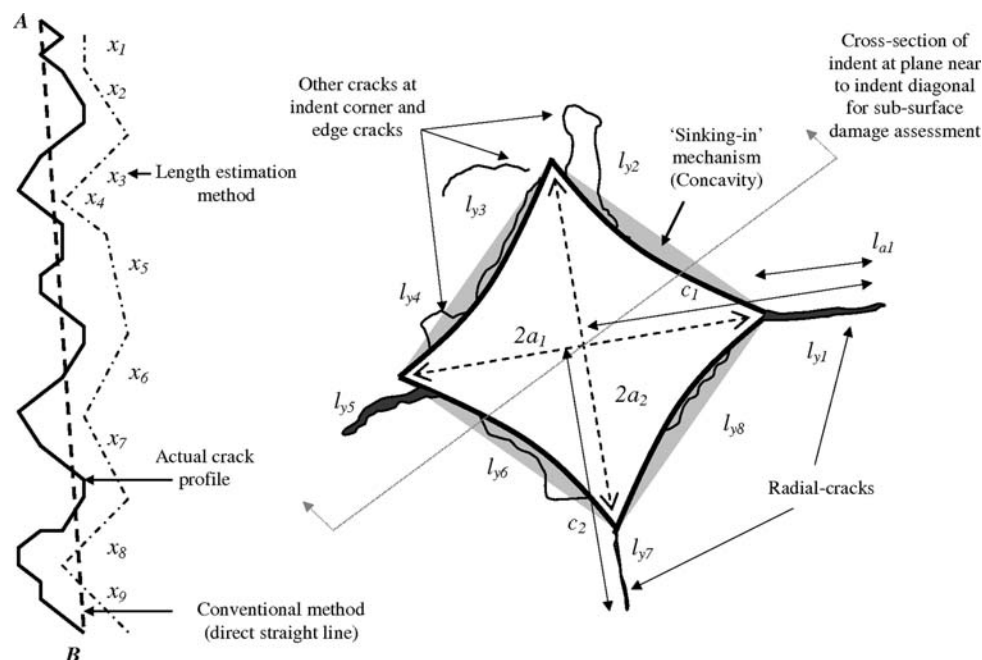
### 2.2 Surface Crack Length Measurement

Figure 1 shows schematically the various types of fracture and methods for measuring the surface crack lengths. Since it is the overall extent of surface cracking during indentation that is said to be indicative of the volumetric damage and to reflect the toughness of the coating (Ref 23), the surface crack length was measured, including the indent diagonal cracks, radial cracks at corners, edge cracks, ring cracks, and other small cracks around the indentation as shown in the schematic diagram in Fig. 1. As illustrated in Fig. 1 (left), crack lengths in the surface plane between points A and B were assessed by adding together the serrated crack path unit lengths,  $l_{yn} = x_1 + x_2 \dots + x_{n-1} + x_n$ . The minimum unit length was determined by the resolution of the micrograph (here 2-3  $\mu\text{m}$ ) and so the method is reproducible and gives a more realistic representation of the total length than the conventional approach. The total surface crack length was then obtained from the sum of the two diagonal sizes plus all the  $n$  resolvable crack lengths:

$$L = 2a + \sum_n l_{yn} \quad (\text{Eq 1})$$

where  $2a$  is the average diagonal size  $= (2a_1 + 2a_2)/2$ .

Also, for comparison with conventional approaches,  $l_a$ , the average of radial crack lengths at the four indent



**Fig. 1** Scheme for measuring the total surface crack length

corners was determined and the dimension,  $c$ , calculated from (Ref 3):

$$c = l_a + a \quad (\text{Eq 2})$$

There are, of course, other subsurface cracks which are not measurable using the optical microscope without sectioning and are therefore not included in the above technique. However, since the primary purpose of measuring surface crack length is to correlate it with AE features for a range of indentation load, this is not an insurmountable difficulty.

### 2.3 AE Data Acquisition System and Signal Processing

The AE recording system consisted of a PC with a 12-bit data acquisition board (PCI-6115, National Instruments Ltd., UK) and a broadband piezo-electric AE sensor based on lead zirconate titanate (Micro-80D, PAC, UK) with associated preamplifier (1220A, PAC, UK). The sensor was 10 mm in diameter and 12 mm high and was held onto the HVOF-coated surface using masking tape and vacuum grease, a method known (e.g., Ref 17) to be reproducible for such semi-static measurements although there is the possibility of reflection of AE waves at the edge of the sample.

Data were sampled at 2.5 MHz so that the full bandwidth of the AE (0.1-1 MHz) could be captured. The preamplifier was set at 60 dB gain and was equipped with an internal band pass filter between 0.1 and 1 MHz. AE was recorded over the frequency range of 0.1-1 MHz at a sampling rate of 2.5 MHz and each record was 2 s long, judged to be sufficient to capture any AE during the indentation itself (typically 0.2-0.4 s) plus any delayed

events after the indenter has settled. Prior to any tests, a sensor was placed on the indenter holder to measure any AE resulting from the operation of the indenter mechanism, but no AE signal was observed. Equally, no AE signal was detected during indenter unloading from any of the indentation loads.

The background noise amplitude was found to be overall 9 mV (at all indentation loads), so an analysis threshold level of 10 mV was chosen to define significant AE activity. Since the interest was in assessing whether the observed AE was likely to be due to a series of fracture and densification events, a simple approach was taken to signal processing. The descent of the indenter to its final rest position is continuous, although the consequent accommodation of the surface material, and hence the events which generate AE, will have a discontinuous element (microfissuring and macroscale cracking). There is likely to be considerable overlap between events and, as mentioned above, waves from a given event may be reflected from the edges and bottom of the specimen and recorded more than once at the sensor. Nevertheless, these effects are likely to affect the generating events from a given indentation and between indentations in a broadly similar way. For this reason, three (not necessarily independent) features were derived from the rectified raw AE record (absolute value of the bipolar raw AE) and aimed at giving a measure of the intensity of cracking. "Ring-down count" ( $R$ ) was obtained from the number of times that the signal amplitude crossed the preset threshold in the positive direction. Similarly, the "total event duration" ( $T$ ) was obtained from the total time that the absolute AE voltage spent above threshold. Again in the interests of obtaining a feature which might be related to a physical quantity, the "AE energy,"  $E$  (in relative units of



voltage  $\times$  time) was then calculated as the area under the absolute of the signal for each of the events:

$$E = \sum_{i=1}^N \int_{t=0}^{T_i} V_{\text{abs}} dt \quad (\text{Eq 3})$$

where  $V_{\text{abs}}$  is the absolute voltage,  $T_i$  is individual event duration, and  $t$  is the time (above threshold) from the beginning of the event.

## 2.4 Specimen Preparation for Subsurface Damage Assessment

Some indentations were sectioned in order to provide a general assessment of the subsurface damage and so enhance understanding of the way in which the material accommodates the indentation. Specifically, sectioning should help identify if classical indentation crack regimes (Ref 24) are present and to what extent surface observations can serve as a measure of the total amount of cracking.

One sample, which included many indentations on one side of the coated surface, was vacuum impregnated (Epovac, Struers Ltd., UK) using a transparent, low viscosity resin (Epofix, Struers Ltd., UK). It was then cut very near to an indentation using a low-speed diamond saw, cutting in the direction from the coating toward the substrate to avoid delamination. Polishing was done carefully to reach the indentation cross section using

increasingly fine grit (with 68, 26, and 15  $\mu\text{m}$  average particle diameters, MD-Piano, Struers Ltd., UK) and a diamond grinding disc. Once the required indentation was reached, the section was finally polished with diamond paste (6, 1, and 0.5  $\mu\text{m}$ ) to enable a sharp cross-sectional view of the indentation subsurface zone. The vacuum impregnation technique (Ref 25, 26) enables the low-viscosity resin to reach most of the surface-linked cracks and pores, and, upon solidification, the resin acts as reinforcement before, during and after sample preparation. It also reduces the possibility of further damage during cutting and polishing of the area of interest.

## 3. Results

The experiments carried out here produced three distinct types of result: mechanical property measurements, metallographic measurements, and AE time series. The mechanical measurements were relatively simple in this case, being confined to the hardness (as defined by indentation dimensions) and the fracture toughness (as determined from cracking patterns), both of which depend on metallographic observations. Representative examples of optical micrographs of the Vickers indentation fracture at four of the 10 loads (49, 196, 343, and 490 N) are shown in Fig. 2 and typical AE signals are shown in Fig. 3.

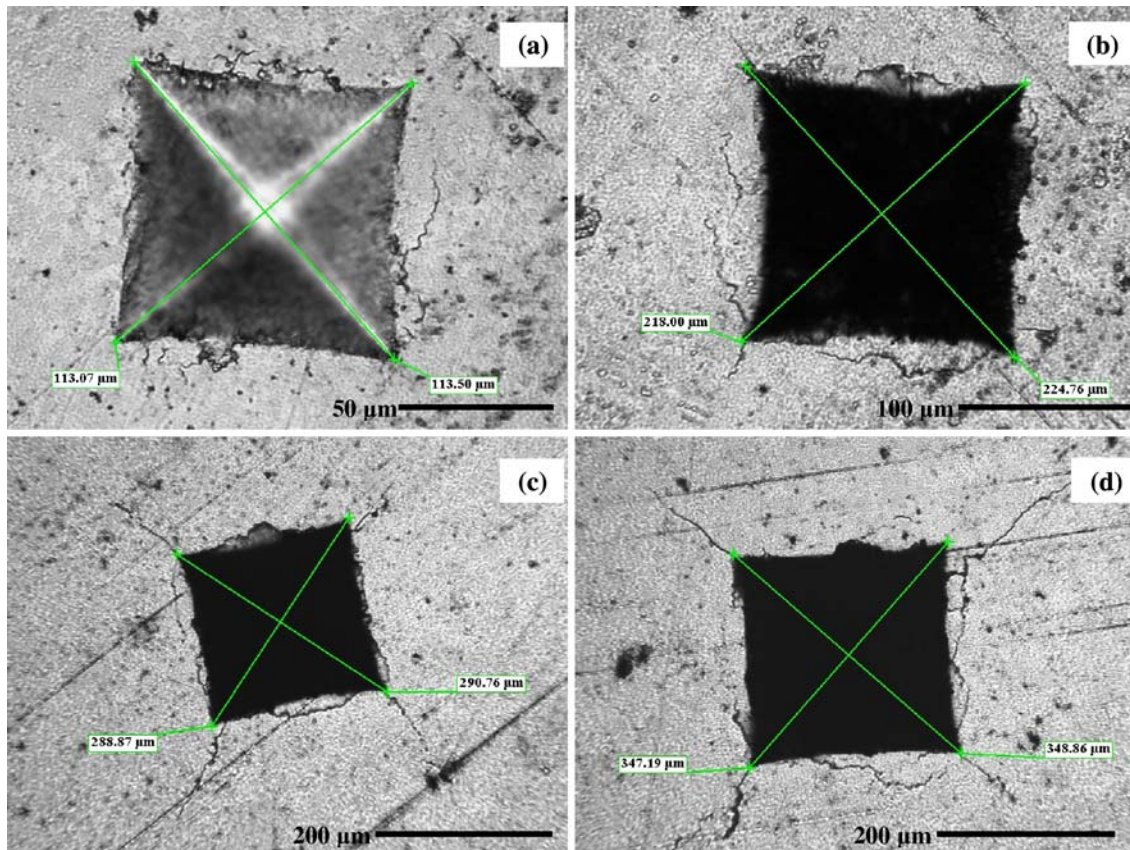


**Fig. 2** Typical Vickers indentation cracking patterns at loads; (a) 49 N, (b) 196 N, (c) 343 N, and (d) 490 N

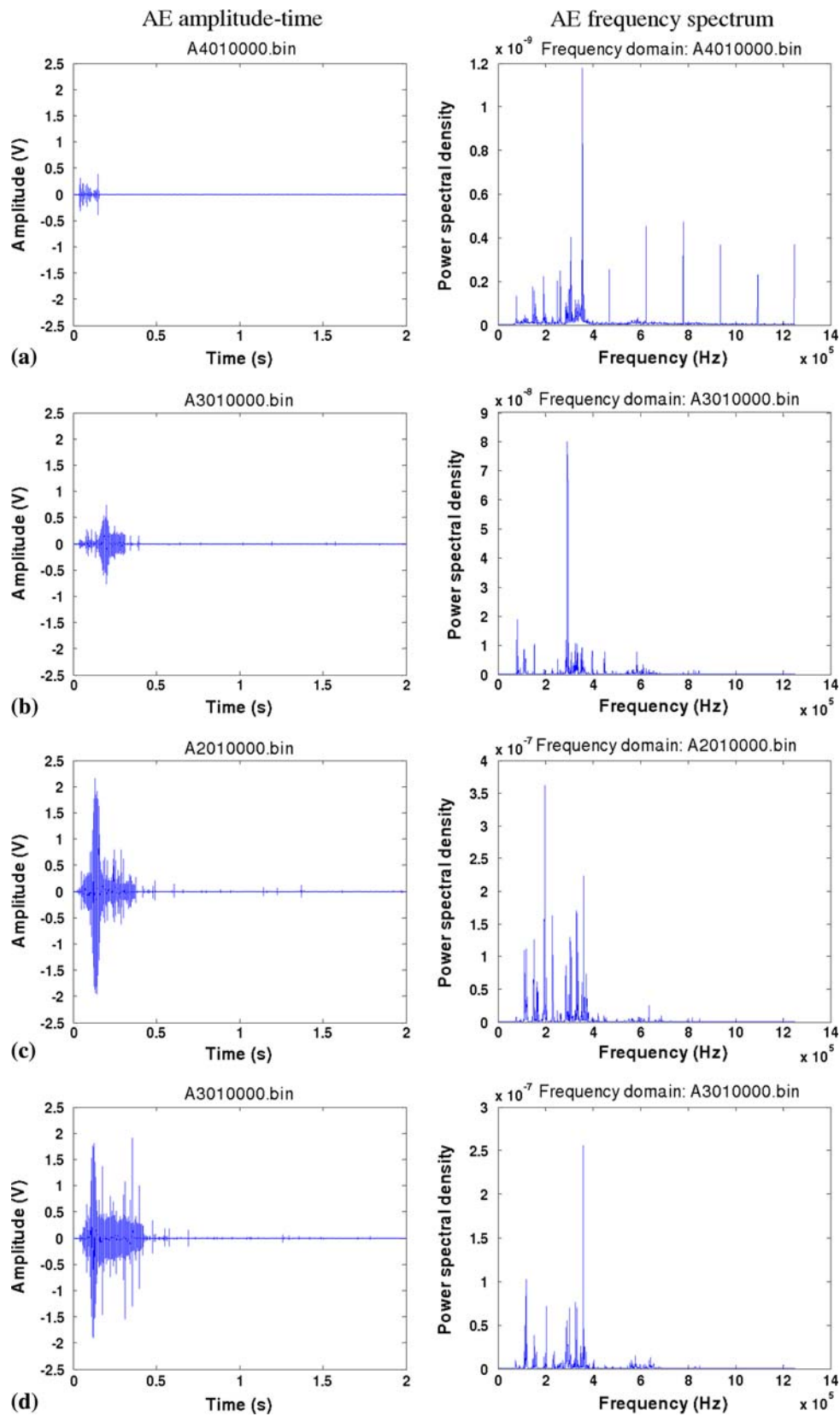


**Fig. 3** Typical AE signal structures (amplitude and frequency) during indentation at loads; (a) 49 N, (b) 196 N, (c) 343 N, and (d) 490 N



### 3.1 Surface and Subsurface Fracture Patterns

The average bulk hardness value measured using the Vickers test over the range of loads (49-490 N) was  $759 \pm 28$  HV with no systematic variation with load. Visible radial cracking from the four corners of the indentation was seen for all loads except the lowest (49 N), at which only minor cracks around the perimeter (edge cracks) and on the surface of the indentation were found. Figure 4 shows cross-sectional views of the damaged region around one indentation at each of the loads 245 and 441 N, where areas with subsurface densification and lateral cracks can be seen. The regions beneath the indenter (densified region) and away from indentation zone can be identified in the micrographs, the porosities immediately under the indenter being 0.15% for the 245 N load and 0.80% for the 441 N load. The corresponding average porosities in the areas just away from the indentation were 4.5% and 3.5% for the 245 N and 441 N loads, respectively. The other mechanism clearly visible in Fig. 4 is subsurface lateral cracking, not dissimilar in its morphology to the edge cracks seen on the outer surface. The extent and orientation of the lateral cracks appears to vary

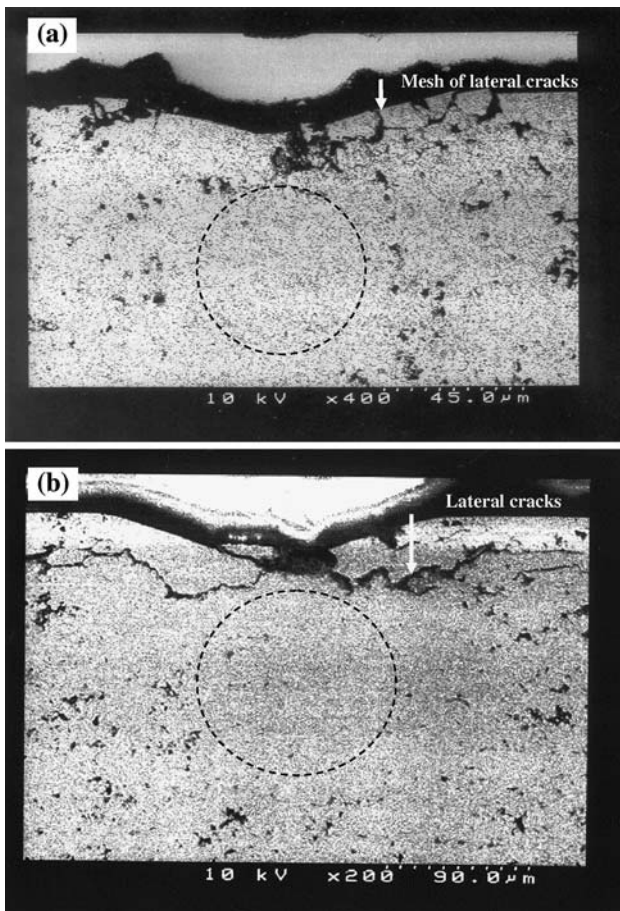


**Fig. 4** SEM images of indent cross sections showing the 'sinking-in' of the indenter and subsurface damage; (a) 245 N and (b) 441 N

with load, judging from the limited evidence that can be seen in Fig. 4. For the 245 N load, the lateral crack had multiple branches both in the lateral and vertical directions and the overall length was almost the size of the indent half diagonal. For the 441 N load, the lateral crack can be seen to emerge onto the surface at a distance over twice the indent diagonal, running at a depth almost equal to the indentation depth. Other events which may appear in the AE record include fracture of individual hard phase particles (Ref 23) beneath the pyramidal surface of the indenter, and a typical case at 441 N load is shown in Fig. 5.

### 3.2 AE Results

As can be seen from Fig. 3, the length of time for which substantial AE was observed during an indentation increased from about 0.1 s at 49 N load to about 0.4 s at 490 N. There was also a considerable increase in amplitude (of about a factor of six) between the extreme values of load. After the main period of emission, the higher load signals continued to exhibit events throughout the 2-s record albeit at much lower amplitude than the main signal.

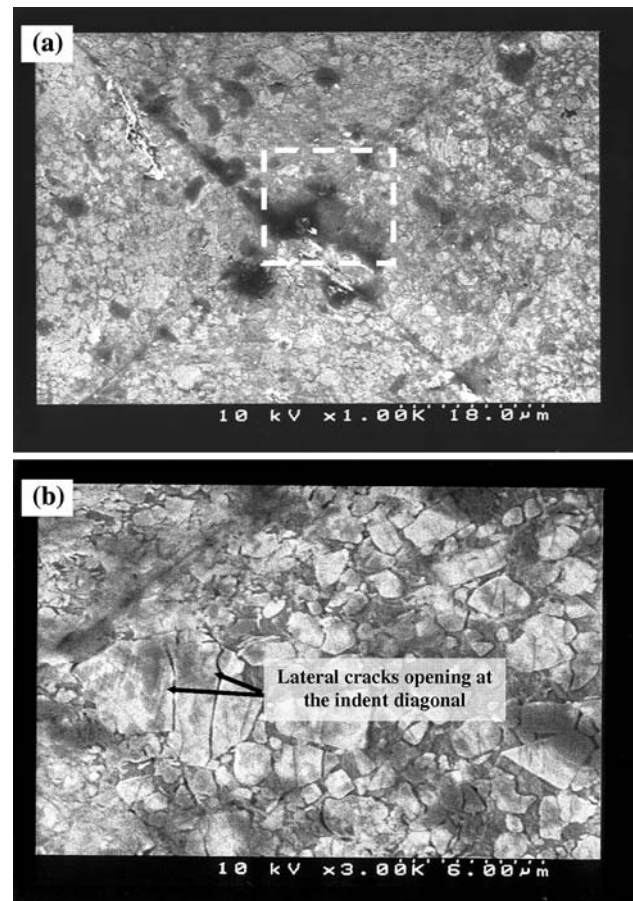


**Fig. 5** SEM images of top view of pyramidal surface of indentation at 441 N load; (a) general view showing indent diagonal and (b) magnified view of boxed area

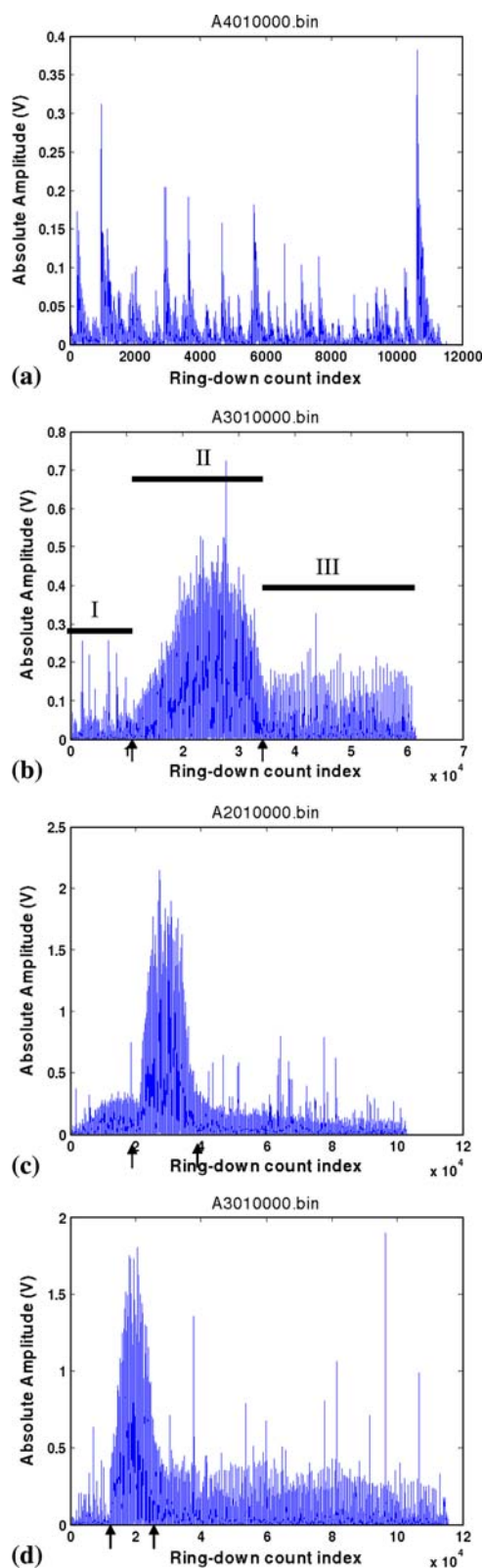


**Fig. 6** Typical magnified absolute AE signals in ring-down count series from Fig. 3; (a) 49 N (Stage I only), (b) 196 N (showing all three stages), (c) 343 N and (d) 490 N, both showing the start and finish of Stage II

As might be expected, the overall power of the frequency spectrum (for the whole AE time series shown in Fig. 3) increased with indentation load. At low loads, much of the power is concentrated around 300-400 kHz, and, as the load increases, the power in the 100 to 250 kHz band generally increases relative to that in the 300-400 kHz band. At all loads, there was a low-power component discernible between 550 and 650 kHz. Other than this, little can be seen immediately to distinguish the spectra apart from a series of large spikes in the spectrum at 49 N load which is attributed to noise and corresponds to a long period in the 2-s record where no events are perceptible above the noise.

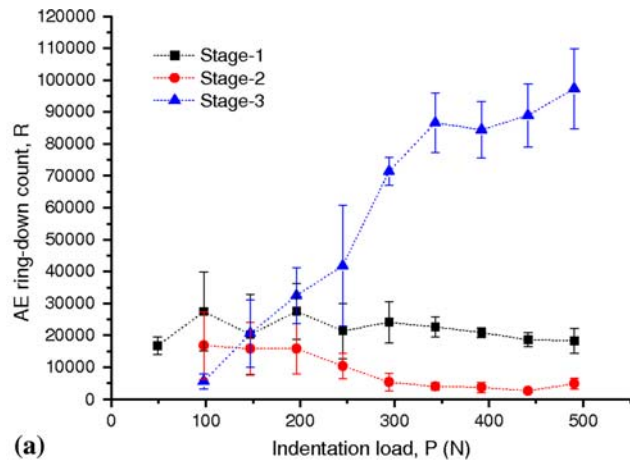
Figure 6 shows the examples from Fig. 3, magnified and presented as ring-down count series, which is a concatenated time-series where only significant events (as defined by the ring-down count described above) are shown. Three distinct stages can be identified from Fig. 6 and 3: Stage I, an initial, relatively low amplitude, discontinuous signal; Stage II, a high amplitude, apparently continuous signal; and Stage III, a low amplitude discontinuous signal with occasional higher amplitude bursts. Figure 6(a) shows Stage I most clearly, and it can be seen that the individual peaks are not evenly spaced in time and are all of different amplitude; similar characteristics were observed for Stage I for all loads. The peak amplitude of Stage II increases rapidly from low-to-moderate loads, and it appears earlier in the record and is of shorter duration as the load increases. In Stage III, the AE amplitude is relatively constant with time and load, although its duration increases with load. For signal processing, the stage boundaries were identified automatically by smoothing the absolute AE signal using the running average of 50 data points and then applying a threshold of 0.2 V, chosen so that its upward crossing identified the Stage I to Stage II boundary and its downward crossing the boundary between Stages II and III.

Figure 7 shows the variation of each of the AE features with indentation load, from which it is clear that Stage III is the dominant component by all three measures at the higher values of load, and that all features increase with load in Stage III. The other stages exhibit a relatively weak variation with load for all three features. Figure 7(b) shows that Stage I always represents a small proportion of the total AE energy, and that Stage II contains the highest proportion at low loads, with Stage III containing the highest at higher loads.

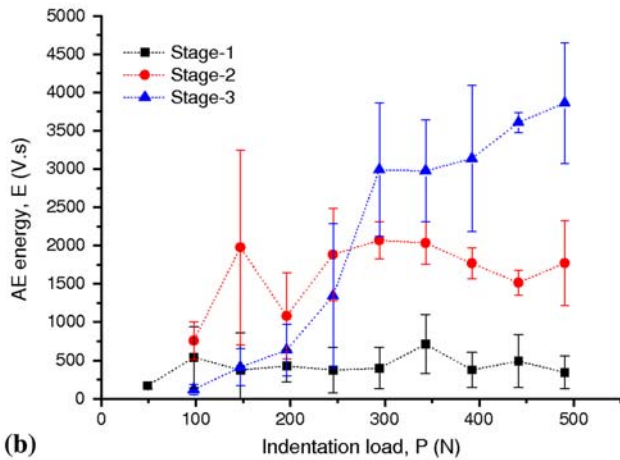
Frequency spectra were taken for each of the three stages for each of the loads, but there was no obvious distinction between these spectra.

## 4. Discussion

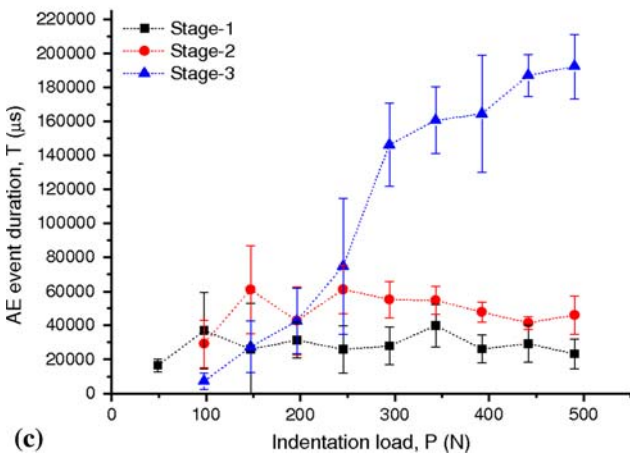
This section is confined to assessing the extent to which AE can be used as a more convenient measure of fracture toughness of coatings than conventional means, which rely upon a metallographic assessment of total crack length.



(a)



(b)



(c)

**Fig. 7** AE features; (a) ring-down count,  $R$ , (b) energy,  $E$ , and (c) event duration,  $T$  vs. indentation load for the stages shown in Fig. 6

Therefore, it is important to establish if the features of the AE are related in a simple way to measures of the crack length, given that it is already established that crack length (however measured) is simply related to fracture toughness. It is important to note that the surface cracking pattern cannot easily be observed during indentation, but

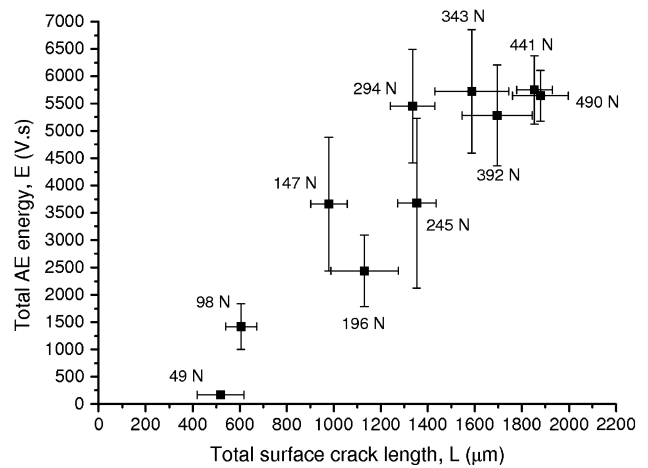


**Fig. 8** Total AE energy plotted against total surface crack length

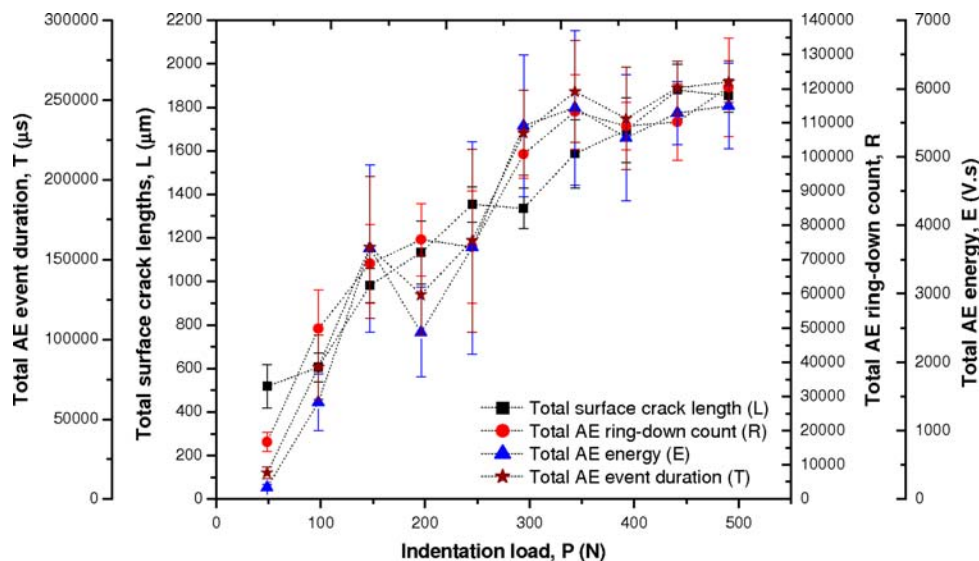
that it is reasonable to suppose that the patterns observed at lower loads correspond to the pattern existing at the early stages of higher loads.

Figure 8 shows total AE energy plotted against total surface crack length, and it can be seen that total AE energy would be a useful surrogate measure for total surface crack length, provided that an appropriate calibration can be obtained. The variability of the AE Energy is a bit greater than of total surface crack length at a given load (error bars in Fig. 8), so it is of interest to consider whether the correlation might be improved by using a different AE feature or by focusing on one of the stages. Figure 9 shows all three AE features plus the total surface crack length plotted against load, with the scales chosen so as to highlight any variations in shape of the four curves. It is evident that all show a similar shape with load, and that there is little to choose between the three features.

All of the feature curves lie below the total surface crack length at the lowest load, giving a strong indication that the AE associated with radial cracking (absent at the lowest load) of a given length is more pronounced than that associated with the other types of crack. As already observed from Fig. 7, Stage III shows the most consistent increase in all of the AE features with load which would suggest that cracking during indentation is better discriminated using Stage III, although Stage II contains the highest intensity of cracking events.

As the 49 N indentation shows, the smaller cracks also generate some AE which can only be associated with Stage I. Irregular networks of smaller cracks not originating at indentation corners have also been observed by others (Ref 23, 27-30) working on thermally sprayed coatings. The metallographic evidence in Fig. 4 and 5 shows cracking of individual particles and densification as the more ductile matrix rearranges itself around the less compliant hard particles as well as the measurable cracking networks. Because the surface is heterogeneous, the early stages of indentation are expected to have an irregular time evolution, as was observed. It is, therefore,





**Fig. 9** Effect of indentation load on total surface crack length and total AE features

likely that Stage I AE is associated with all of the accommodation processes which take place before the first radial cracks form. AE from such sources is likely also to continue through Stages II and III, but will be swamped by the stronger sources due to radial cracking. This explanation is consistent with the observation (Fig. 7) that Stage I AE is independent of load, since the first radial cracks should start to occur once the indenter has reached a given depth, irrespective of the applied load. If the indenter does not reach this depth, corresponding to the indentation size at a certain critical load for the coating, then radial cracks will not appear. Thus, the critical load for the coating under study is between 49 and 98 N.

Above the critical impression size, the coating can no longer accommodate the impression size by densification and local cracking, and so radial cracks emanate from the indentation corners. Stage II clearly involves breakthrough of the indenter into the surface of the coating which is consistent with the Stage II AE features being relatively insensitive to load (Fig. 7) and the duration of the breakthrough being shorter at higher loads (Fig. 6). A higher intensity of individual fracture events during breakthrough at higher loads also accounts for the (apparent) reduction in Stage III ring-down count with increasing load (Fig. 7a).

According to the various published analyses of indentation of brittle materials, the main types of cracking observed are either surface-radial cracks (Palmqvist cracks), or radial-median cracks (half-penny cracks). Nihara et al. (Ref 3) have distinguished between the two in terms of the conventional dimensions  $a$ ,  $l_a$ , and  $c$  of Eq 2: Palmqvist cracks,  $l_a/a \leq 2.5$  or  $c/a \leq 2.5$  and half-penny cracks,  $c/a \geq 2.5$ . In this study, the average value of  $l_a/a$  was around 0.4 and  $c/a$  was around 1.4, and so the crack regime should be of the Palmqvist type, and this is supported by the absence of subsurface radial-median cracks in the SEM images (Fig. 4). Shetty et al. (Ref 5)

have devised an empirical model for Palmqvist cracks, which allows the fracture toughness of the coating to be determined from the load and crack dimensions:

$$K_{Ic} = 0.0319 \left[ \frac{P}{a\sqrt{l_a}} \right] \quad (\text{Eq 4})$$

where  $P$  is the indentation load (in Newtons), and  $a$  and  $l_a$  are the conventional dimensions, both in meters. Using the dimensions derived for all indentations at all loads (except 49 N, where there were no radial corner cracks), the average value of fracture toughness, according to this measure, was  $8.81 \pm 0.47 \text{ MPa m}^{1/2}$ . For the same coating material (HVOF as-sprayed WC-12%Co), Lima et al. (Ref 12) have determined a value of  $5.1 \pm 0.7 \text{ MPa m}^{1/2}$  (using the Shetty et al. model, Ref 5) or  $4 \pm 1 \text{ MPa m}^{1/2}$  (using the Nihara model, Ref 4).

In their review of practice on relating fracture toughness to cracking patterns observed following indentation, Ponton and Rawlings (Ref 24) have developed a series of generic correlation equations (based on both the Palmqvist and radial-median crack models), between fracture toughness and the conventional measures (Eq 2), surface radial crack length  $l$ , indent half-diagonal  $a$ , and indentation load  $P$ . They have recommended 'generic equations' (GEs) which summarize much of the practice observed. Here, the GE has been modified to replace the average radial-corner crack length  $l_a$ , with either the total surface crack length  $L$ , the total AE ring-down count  $R$ , the total AE energy  $E$ , or the total AE event duration  $T$  to give a modified generic equation for AE-based fracture toughness estimation ( $K_{AE}$ ) for Palmqvist-type cracks:

$$K_{AE} = k_1 \left[ \frac{P}{a\sqrt{X}} \right] \quad (\text{Eq 5})$$

where  $X$  is one of variables,  $L$ ,  $R$ ,  $E$  or  $T$  and  $k_1$  is an empirical constant which can, in principle, be

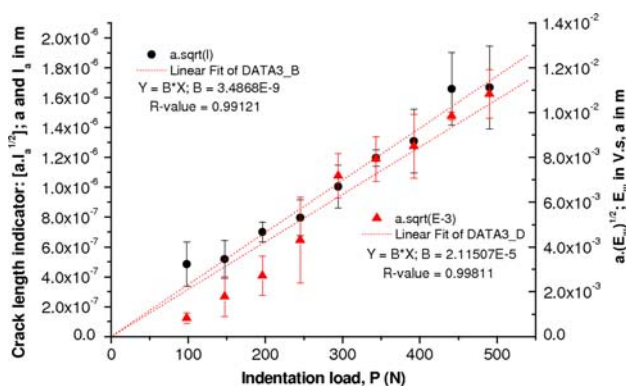


**Fig. 10** Plots of Eq 5 with the variable  $X$  given by radial crack length,  $l_a$  or Stage III AE energy,  $E_{III}$

determined for any given indenter-specimen-AE system combination.

Plotting of  $a \cdot X^{1/2}$  against  $P$  should, according to Eq 5, produce a straight line if the measure  $X$  is suitable for determining fracture toughness, the inverse of the slope being  $K_{AE}/k_1$ . The correlation coefficients for such plots for  $L$ ,  $R$ ,  $E$ , and  $T$ , respectively, were found to be 0.9957, 0.9919, 0.9931, and 0.9959, indicating that the AE measures are about as good as total surface crack length in determining fracture toughness.

Figure 10 shows the Shetty et al. (Ref 5) equation (i.e.,  $X$  is given by  $l_a$ ), where it can be seen that the correlation ( $r=0.9912$ ) is not as good as for total surface crack length, even with the lowest load excluded, as it is in Fig. 10. Also shown in Fig. 10 is the Stage III AE energy, which gives a superior correlation to any of the other AE indicators or indicators of crack length ( $r=0.9981$ ). It might also be noted that the Stage III AE energy lies below the best-fit line for all the lower loads, reflecting the fact that Stage II is the dominant component of AE energy at low loads.

Although care was taken to avoid aggressive polishing during sample preparation; however, no matter how carefully polishing is done, this will inevitably induce small changes to the near-surface residual stress pattern (Ref 31). The relative changes caused by polishing in AE and cracking behavior, however, would be minimal in this comparative investigation as both are interrelated phenomenon.

## 5. Conclusions

This study has focused on assessing whether AE monitoring during indentation can be used as an indirect measure of fracture toughness in competition with the conventional approach (for brittle materials) of using surface cracking patterns observed after indentation. It has been found that:

1. All of the AE features can be used as a surrogate for total surface crack length and total surface crack

length is a superior measure to the conventional average diagonal crack length for the coating studied.

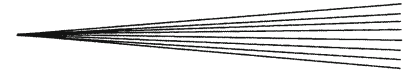
2. The AE recorded during macroindentation shows three distinct stages, the onset of the second marking the critical indentation size (for the specific coating) where radial cracks begin to form. Stage III is associated with the continuation of all mechanisms of accommodation as the indenter descends further into the coating, and therefore changes significantly with load.

## Acknowledgments

The authors would like to thank Deloro Stellite Ltd., UK for supplying the as-sprayed HVOF WC-12%Co coated samples for this study. The authors would also like to express their thanks to Metallurgist, Bill Taylor, at Struers Ltd., UK, for his support in the metallurgical preparation of the cross section of the Vickers indent for subsurface damage assessment.

## References

1. J. Lankford, Indentation Microfracture in Palmqvist Crack Regimes: Implications for Fracture Toughness Evaluation by the Indentation Method, *J. Mater. Sci. Lett.*, 1982, **1**, p 493-495
2. B.R. Lawn and A.G. Evans, A Model for Crack Initiation in Elastic/Plastic Indentation Fields, *J. Mater. Sci.*, 1977, **12**, p 2195-2199
3. K. Nihara, R. Morena, and D.P. Hasselman, Evaluation of  $K_{IC}$  of Brittle Solids by the Indentation Method with Low Crack-to-Indent Ratios, *J. Mater. Sci. Lett.*, 1982, **1**, p 13-16
4. K. Nihara, A Fracture Mechanics Analysis of Indentation-Induced Palmqvist Crack in Ceramics, *J. Mater. Sci. Lett.*, 1983, **2**, p 221-223
5. D.K. Shetty, I.G. Wright, P.N. Mincer, and A.H. Clauer, Indentation Fracture of WC-Co Cermets, *J. Mater. Sci.*, 1985, **20**, p 1873-1882
6. K.M. Liang, G. Orange, and G. Fantozzi, Evaluation by Indentation of Fracture Toughness of Ceramic Materials, *J. Mater. Sci.*, 1990, **25**, p 207-214
7. C.K. Lin, C.C. Lin, and C.C. Berndt, Simulation of Hardness on Plasma-Sprayed Coatings, *J. Am. Ceram. Soc.*, 1995, **78**(5), p 1406-1410
8. C.K. Lin and C.C. Berndt, Statistical Analysis of Microhardness Variations in Thermal Spray Coatings, *J. Mater. Sci.*, 1995, **30**, p 111-117
9. S. Ghosh, S. Das, T.K. Bandyopadhyay, P.P. Bandyopadhyay, and A.B. Chattopadhyay, Indentation Responses of Plasma Sprayed Ceramic Coatings, *J. Mater. Sci.*, 2003, **38**, p 1565-1572
10. E.L. Cantera and B.G. Mellor, Fracture Toughness and Crack Morphologies in Eroded WC-Co-Cr Thermally Sprayed Coatings, *Mater. Lett.*, 1998, **37**, p 201-210
11. J. Lesage and D. Chicot, Role of Residual Stresses on Interface Toughness of Thermally Sprayed Coatings, *Thin Solid Films*, 2002, **415**, p 143-150
12. M.M. Lima, C. Godoy, J.C. Avelar-Batista, and P.J. Modenesi, Toughness Evaluation of HVOF WC-Co Coatings using Non-Linear Regression Analysis, *Mater. Sci. Eng. A*, 2003, **357**, p 337-345
13. M.M. Lima, C. Godoy, P.J. Modenesi, J.C. Avelar-Batista, A. Davison, and A. Matthews, Coating Fracture Toughness determined by Vickers Indentation: An Important Parameter in Cavitation Erosion Resistance of WC-Co Thermally Sprayed Coatings, *Surf. Coat. Technol.*, 2004, **177-178**, p 489-496



14. C.M. Nygard, K.W. White, and K. Ravi-Chandar, Strength of HVOF Coating-Substrate Interface, *Thin Solid Films*, 1998, **332**, p 185-188 ((US Patent no. 6,581,446 B1, 24th June 2003))
15. C.B. Scruby, An Introduction to Acoustic Emission, *J. Phys. E Sci. Instrum.*, 1987, **20**, p 946-953
16. R.L. Reuben, The Role of Acoustic Emission in Industrial Condition Monitoring, *Int. J. Condition Monitor. Diagnost. Eng. Manag. COMADEM*, 1998, **1**(4), p 35-46
17. J.A. Steel and R.L. Reuben, Recent Developments in Monitoring of Engines Using Acoustic Emission, *J. Strain Anal.*, 2005, **40**(1), p 45-57
18. S. Safai, H. Herman, and K. Ono, Acoustic Emission Study of Thermal-Sprayed Oxide Coatings, *Am. Ceram. Soc. Bull.*, 1979, **58**, p 624
19. S.L. Ajit Prasad, M.M. Mayuram, and R. Krishnamurthy, Response of Plasma-Sprayed Alumina-Titania Composites to Static Indentation Process, *Mater. Lett.*, 1999, **41**, p 234-240
20. K. Vijayakumar, A.K. Sharma, M.M. Mayuram, and R. Krishnamurthy, Response of Plasma-Sprayed Alumina-Titania Ceramic Composite to High-Frequency Impact Loading, *Mater. Lett.*, 2002, **54**, p 403-413
21. U. Senturk, R.S. Lima, C.R.C. Lima, and C.C. Berndt, Deformation of Plasma Sprayed Thermal Barrier Coatings, *Trans. ASME J. Eng. Gas Turbines Power*, 2000, **122**, p 387-392
22. R. Ahmed, H. Yu, S. Stewart, L. Edwards, and J. Santisteban, Residual Strain Measurement in Thermal Spray Cermet Coatings via Neutron Diffraction, *ASME J. Tribol.*, 2007, **129**, p 411-418
23. M. Factor and I. Roman, Microhardness as a Simple Means of Estimating Relative Wear Resistance of Carbide Thermal Spray Coatings: Part 1. Wear Resistance of Cemented Carbide Coatings, *J. Therm. Spray Technol.*, 2002, **11**(4), p 468-481
24. C.B. Ponton and R.D. Rawlings, Vickers Indentation Fracture Toughness Test: Part 1. Review of Literature and Formulation of Standardised Indentation Toughness Equations, *Mater. Sci. Technol.*, 1989, **5**, p 865-872
25. "Standard Guide for Metallographic Preparation of Thermal Sprayed Coatings," ASTM E1920-97, *Annual Book of ASTM Standards*, ASTM, p 1055-1059
26. J. Karthikeyan, A.K. Sinha, and A.R. Biswas, Impregnation of Thermally Sprayed Coatings for Microstructural Studies, *J. Therm. Spray Technol.*, 1996, **5**(1), p 74-78
27. P. Ostojic and R. McPherson, Indentation Toughness Testing of Plasma Sprayed Coatings, *Mater. Forum*, 1987, **10**(4), p 247-255
28. H. Luo, D. Goberman, L. Shaw, and M. Gell, Indentation Fracture Behaviour of Plasma-Sprayed Nanostructured Al<sub>2</sub>O<sub>3</sub>-13wt. %TiO<sub>2</sub> Coatings, *Mater. Sci. Eng. A*, 2003, **346**, p 237-245
29. A. Roman, D. Chicot, and J. Lesage, Indentation Test to Determine the Fracture Toughness of Nickel Phosphorus Coatings, *Surf. Coat. Technol.*, 2002, **155**, p 161-168
30. V. Stoica, R. Ahmed, T. Itsukaichi, and S. Tobe, Sliding Wear Evaluation of Hot Isostatically Pressed (HIPed) Thermal Spray Cermet Coatings, *Wear*, 2004, **257**, p 1103-1124
31. R. Ahmed, H. Yu, L. Edwards, and J. Santisteban, Neutron Diffraction Residual Strain Measurements in Post-treated Thermal Spray Cermet Coatings, *Mater. Sci. Eng. A*, 2008, **498**, p 191-202